

pubs.acs.org/JACS Article

# Why Oxygen Increases Carrier Lifetimes but Accelerates Degradation of CH<sub>3</sub>NH<sub>3</sub>Pbl<sub>3</sub> under Light Irradiation: Time-Domain Ab Initio Analysis

Jinlu He, Wei-Hai Fang, Run Long,\* and Oleg V. Prezhdo



Cite This: J. Am. Chem. Soc. 2020, 142, 14664-14673



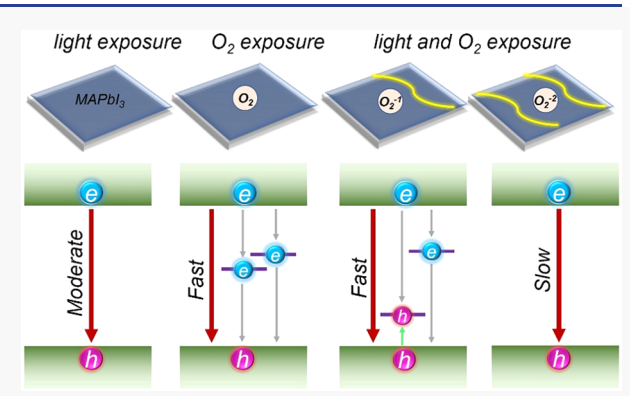
**ACCESS** 

III Metrics & More

Article Recommendations

S Supporting Information

ABSTRACT: Exposure to oxygen and light undermines chemical stability of metal halide perovskites, while it surprisingly improves their optical properties. Focusing on CH<sub>3</sub>NH<sub>3</sub>PbI<sub>3</sub>, we demonstrate that material degradation and charge carrier lifetimes depend strongly on the oxidation state of the oxygen species. Nonadiabatic molecular dynamics simulations combined with time-domain density functional theory show that a neutral oxygen molecule has little influence on the perovskite stability, while the superoxide and the peroxide accelerate degradation by breaking Pb–I chemical bonds and enhancing atomic fluctuations. Creating electron and/or hole traps, the neutral oxygen and the superoxide decrease charge carrier lifetimes by over 1 and 2 orders of magnitude, respectively. Importantly, photoinduced reduction of oxygen to the peroxide eliminates trap states and extends carrier lifetimes by more than a factor of 2 because it decreases the



nonadiabatic coupling and shortens quantum coherence. The simulations indicate that the superoxide should be strongly avoided, for example, by full reduction to the peroxide because it causes simultaneous degradation of perovskite stability and optical properties. The detailed simulations rationalize the complex interplay between the influence of atmosphere and light on perovskite performance, apply to other solar cell materials exposed to natural elements, and provide valuable insights into design of high-performance solar cells.

### 1. INTRODUCTION

Hybrid inorganic-organic perovskites (HIOPs) hold great promise for solar cell applications. The achievement of the record power conversion efficiencies (PEC) of up to 25.2%, which is comparable to the PEC of commercial silicon solar cells, took just a decade.<sup>2</sup> The rapid growth of PEC is attributed to the suitable bandgap,<sup>3</sup> high light absorption coefficient,<sup>4</sup> and large charge carrier diffusion lengths.<sup>3,5,6</sup> The appealing advantages stimulated applications into other optoelectronic devices, such as light-emitting diodes and lasers.8 At the same time, HIOPs such as MAPbI<sub>3</sub> (MA = CH<sub>3</sub>NH<sub>3</sub><sup>+</sup>) exhibit low stability against high temperature, 9,10 humidity, 10,11 light irradiation, 12,13 and oxygen atmosphere. 14-16 Even though oxygen accelerates MAPbI<sub>3</sub> degradation, it can suppress nonradiative electron-hole recombination and improve the performance of solar cells and other optoelectronic devices, as demonstrated experimentally. 177 Long-lived charge carriers are particularly important for enhancing the PEC of solar cells because nonradiative recombination is the major source for energy and current

Haque and coauthors demonstrated that the degradation of MAPbI<sub>3</sub> upon exposure to oxygen was accelerated with light

soaking, while no degradation was found in the dark environment. Similar phenomena were reported by other groups. The oxygen-mediated HOIP degradation is accelerated upon exposure to light because participation of one or two photoexcited electrons can convert the oxygen molecule into superoxide  $(O_2^{-1})$  and peroxide  $(O_2^{-2} = 2O^{-1})$ , facilitating formation of O–Pb bonds by dissociating  $O_2$  and ultimately breaking the local Pb–I octahedral structure. Theoretical studies indicated that photoexcited electrons can transfer from MAPbI<sub>3</sub> to adsorbed oxygen molecules and that superoxide can form spontaneously and cause MAPbI<sub>3</sub> damage. Davies and coauthors showed that superoxide formation was dependent on several factors including oxygen diffusion, defect density, sample morphology, and grain size. Other groups claimed that peroxide was the final product of

Received: June 23, 2020 Published: July 31, 2020





oxygen in the presence of excess electrons since it was an energetically favorable species compared to the superoxide.<sup>22</sup>

Although oxygen decreases the chemical stability of perovskites in the presence of light irradiation, it improves perovskite optical properties. 17-20 Using time-resolved luminescence microscopy, Tian et al. reported that oxygen could increase the photoluminescence (PL) quantum yield by more than 3 orders of magnitude and extend the PL lifetime of MAPbI<sub>3</sub>. The same group demonstrated further that transfer of electron from perovskite to an adsorbed or embedded oxygen could suppress deep trap states at both surface and bulk of MAPbI<sub>3</sub> and enhance the PL intensity, <sup>19</sup> hypothesizing that formation of oxygen-related species eliminates defects and reduces nonradiative charge recombination. Similarity, other groups reported that the PL intensity of MAPbI3 was substantially enhanced under an oxygen atmosphere and light irradiation, 18 while the PL intensity was suppressed after turning off the illumination because charge traps reactivate. Thus, the coexistence of oxygen and light soaking creates favorable conditions for improving the optical performance of perovskites.<sup>20</sup> A detailed understanding of the positive and negative effects of various oxygen species on the perovskite optoelectronic properties can be best provided by quantum dynamics simulations at the atomistic level of description.

Motivated by both experimental and theoretical works,  $^{14,15,18-20,22,23,25}$  we carry out ab initio nonadiabatic (NA) molecular dynamics (MD) $^{26-28}$  simulations combined with time-dependent density functional theory (TDDFT) $^{29}$  to investigate the photoinduced charge trapping and recombination dynamics (depicted in Figure 1) in bulk MAPbI<sub>3</sub> and MAPbI<sub>3</sub> containing various interstitial oxygen species (O<sub>2</sub>, O<sub>2</sub> $^{-1}$ , and O<sub>2</sub> $^{-2}$ ). The simulations show that the neutral oxygen molecule interacts weakly with MAPbI<sub>3</sub>, having negligible influence on the perovskite chemical stability. However, molecular oxygen creates two electron trap states, providing

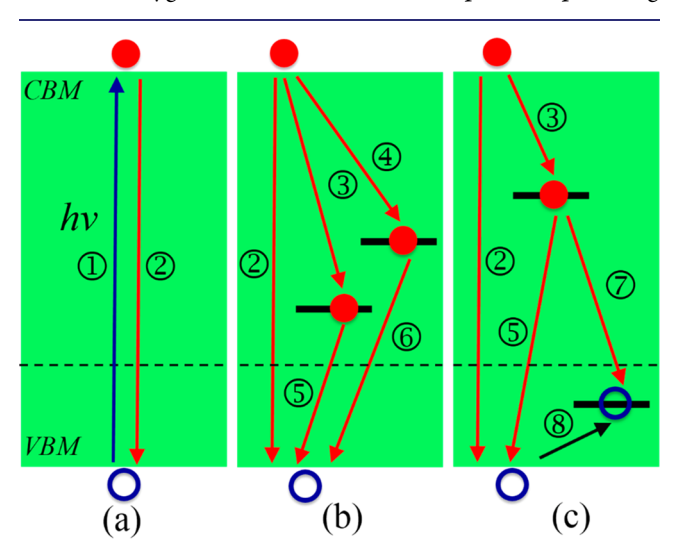


**Figure 1.** Charge carrier trapping and recombination processes in (a) pristine MAPbI<sub>3</sub> and  $O_2^{-2}$ , (b)  $O_2$ , and (c)  $O_2^{-1}$ . ① Absorption of a photon promotes an electron from the VBM to CBM. ② Phononassisted nonradiative electron—hole recombination across the CBM–VBM energy gap. ③,④ Electron trapping from CBM to midgap states. ⑤,⑥ Recombination of trapped electrons with holes in the VBM. ⑦ Recombination of trapped electrons with trapped holes. ⑧ Hole trapping from VBM to the midgap state. The dashed lines denote the Fermi level.

additional nonradiative relaxation pathways (Figure 1b) and accelerating charge recombination by more than an order of magnitude. Because the electron trap states are energetically far from the conduction band (CB), both trap assisted and direct recombination between CB and valence band (VB) edges occur in parallel. Once electrons populate the trap states, they recombine with holes on the sub-100 ps time scale. In contrast, superoxide  $(O_2^{-1})$  and peroxide  $(O_2^{-2})$  degrade the perovskite by breaking Pb-I chemical bonds and forming O-Pb bonds. The superoxide and peroxide systems exhibit large atomic fluctuations, creating conditions for chemical decomposition of the perovskites. The bonds in the superoxide are undercoordinated, and as a consequence, the superoxide creates both electron and hole traps (Figure 1c). There exist no uncoordinated bonds in the peroxide, and the midgap states are eliminated (Figure 1a). The presence of electron and hole traps in the  $O_2^{-1}$  system promotes very rapid nonradiative charge recombination, which is 2 orders of magnitude faster than in the pristine perovskite and which is facilitated by rapid hole trapping. The carrier recombination takes place within 2 ns in the pristine MAPbI<sub>3</sub>, agreeing with experiment.<sup>30</sup> Interestingly, peroxide extends the carrier lifetime more than 2-fold because it decreases the NA coupling and shortens the quantum coherence time, while creating no midgap states. The simulations rationalize the mechanisms underlying the undermined chemical stability and the extended charge carrier lifetimes of perovskites exposed to oxygen and light, resolve the experimental puzzles, and indicate strongly that the superoxide should be avoided because it causes simultaneous degradation of perovskite stability and optical properties. The obtained results apply to other energy conversion materials, which operate in ambient conditions and are subjected to both oxygen and light.

## 2. THEORETICAL METHODOLOGY

The simulations of the charge trapping and recombination processes are performed by using the decoherence induced surface hopping (DISH)<sup>31</sup> NAMD<sup>26–28</sup> approach implemented within real-time TDDFT<sup>29</sup> in the Kohn–Sham representation.<sup>32</sup> The lighter and faster electrons are treated quantum mechanically, while the heavier and slower nuclei are described semiclassically. This approach has been used extensively and successfully to study excited-state dynamics in a broad range of materials,<sup>25,33–57</sup> such as perovskites,<sup>25,33–42</sup> silicon,<sup>43</sup> and transition metal dichalcogenides.<sup>44,57</sup> The detailed description of the approach can be found in refs 26 and 27.

The 192-atom  $2 \times 2 \times 1$  supercell in tetragonal phase<sup>58</sup> is taken from our previous work to represent the pristine MAPbI<sub>3</sub>. 42 The O<sub>2</sub> system is created by adding an interstitial oxygen molecule into the pristine MAPbI<sub>3</sub>. Adding one or two extra electrons into the  $O_2$  system produces the  $O_2^{-1}$  and  $O_2^{-2}$ systems, respectively. The spin-polarized DFT calculations, including geometry optimization, adiabatic MD, and NA coupling, are performed using the Vienna Ab initio Simulation Package (VASP).<sup>59</sup> The Perdew-Burke-Ernzerhof (PBE) exchange—correlation functional<sup>60</sup> and the projector augmented wave method for electron-ion core interactions with a plane-wave energy cutoff of 400 eV are used. A 2  $\times$  2  $\times$ 2 Γ-centered Monkhorst-Pack k-point mesh is used for the geometry optimization and electronic structure calculations. 62 The weak van der Waals interactions are described by using the Grimme DFT-D3 approach.<sup>63</sup> The optimized geometries

are heated to 300 K via repeated velocity rescaling lasting for 2 ps. Then, 4 ps MD trajectories are obtained in the microcanonical ensemble with a 1 fs atomic time step. The NA coupling calculations are performed at the  $\Gamma$ -point because the direct bandgaps of the four systems are at the  $\Gamma$ -point. The first 1000 geometries are chosen as initial conditions for the NAMD simulations of the charge trapping and recombination using the PYthon eXtension for Ab Initio Dynamics (PYXAID) code.  $^{26,27}$ 

## 3. RESULTS AND DISCUSSION

We start by discussing geometric properties of the pristine MAPbI<sub>3</sub>,  $O_2$ ,  $O_2^{-1}$ , and  $O_2^{-2}$  systems. Then, we analyze their electronic structure and electron—vibrational interactions. Finally, we study the charge trapping and recombination dynamics in the four systems to reveal the origin of the extended charge carrier lifetimes observed in the experiments.  $^{17-20}$ 

**3.1. Geometric Structure.** The optimized geometries of the pristine MAPbI<sub>3</sub>,  $O_2$ ,  $O_2^{-1}$ , and  $O_2^{-2}$  systems are shown in Figure 2. The interstitial oxygen molecule and the nearest lead

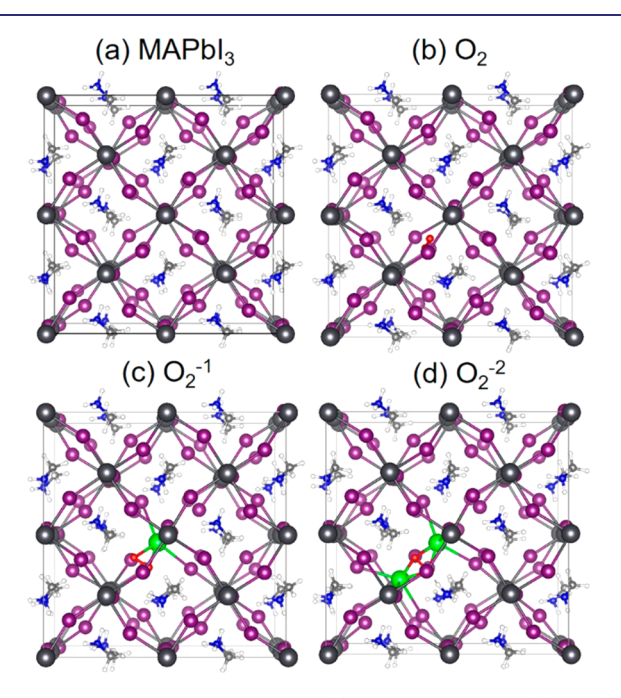


**Figure 2.** Optimized geometries of (a) pristine MAPbI<sub>3</sub>, (b)  $O_2$ , (c)  $O_2^{-1}$ , and (d)  $O_2^{-2}$  systems. The interstitial oxygen molecule and the lead atoms chemically bound to the molecule are highlighted by the red and green spheres.

atoms are denoted by the red and green spheres. Compared to the pristine MAPbI<sub>3</sub> (Figure 2a), the geometry of the  $O_2$  system remains intact because the neutral oxygen molecule interacts weakly with the perovskite via physical adsorption at 0 K and induces virtually no changes in the coordinates of the surrounding lead atoms (Figure 2b). Even though the interaction between the  $O_2$  molecule and the perovskite is weak, the O–O bond length is greater than that in the free oxygen molecule (1.208 Å), since large electronegativity of oxygen favors attraction to the positive lead ions. Once the neutral oxygen molecule accepts an electron from the excited MAPbI<sub>3</sub>, it converts into the superoxide  $O_2^{-1}$  species, and the O–O bond elongates significantly to 1.361 Å. The oxygen

atoms get closer to the nearest lead ion, breaking one I–Pb chemical bond and forming two O–Pb (Figure 2c). The two oxygen atoms become undercoordinated and mobile. Once the  $\rm O_2^{-1}$  species accepts another electron, it converts to the peroxide  $\rm O_2^{-2}$ . The O–O distance increases further to 1.522 Å due to destabilization of the O–O bond and repulsion between the negatively charged oxygens. The  $\rm O_2^{-2}$  negative charge and bond expansion increases interaction with the surrounding Pb atoms. Compared to  $\rm O_2^{1-}$ , which interacts strongly with a single Pb,  $\rm O_2^{-2}$  is capable to interact with two Pb atoms, break two I–Pb bonds, and form four O–Pb bonds (Figure 2d). Both oxygen atoms are fully coordinated in the peroxide. The geometric structure analysis indicated that both superoxide and peroxide species undermine perovskite stability.

The above analysis demonstrates that the O–O bond extension leading to oxygen molecule dissociation and formation of new O–Pb chemical bonds constitute the key step of perovskite degradation. This process is enhanced by  $O_2$  reduction to the superoxide and peroxide. To examine how thermal fluctuations affect perovskite stability, we computed evolution of the O–O distances in the  $O_2$ ,  $O_2^{-1}$ , and  $O_2^{-2}$  systems (Figure 3). The O–O distances at 0 K in the

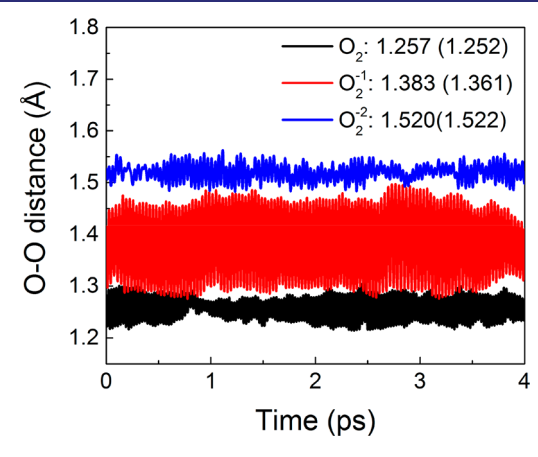


**Figure 3.** Evolution of the O–O distances in the  $O_2$ ,  $O_2^{-1}$ , and  $O_2^{-2}$  systems. The numbers outside and inside the parentheses denote the canonically averaged and optimized distances, respectively. The superoxide species undergoes the largest fluctuation, indicative of its chemical instability.

optimized structures and the canonically averaged values at 300 K are presented inside and outside the parentheses in Figure 3. Though the canonically averaged O–O distances change little compared to 0 K, the distances fluctuate significantly at room temperature. The superoxide species undergoes the largest fluctuation by far because the oxygen atoms are undercoordinated. The O–O distance fluctuates much less in the peroxide because the oxygens are fully coordinated. Instead of undergoing large-scale O–O stretching, the oxygen atoms in both  $O_2$  and  $O_2^{-2}$  move together as in stable species. The strong O–O distance fluctuation of the superoxide indicates that it is chemically reactive and, in particular, that it can be reduced to peroxide by attracting another electron. This observation is consistent with previous theoretical reports.  $^{22}$ 

It is necessary to emphasize that the MD analysis provides new, important information compared to the optimized geometries and even reverses the trend deduced from the 0 K data. Thus, the optimized geometries suggest that the peroxide  ${\rm O_2}^{-2}$  should be more detrimental for the perovskite chemical stability than the superoxide  ${\rm O_2}^{-1}$  because the peroxide has a longer O–O bond and interacts with more Pb atoms. However, the MD trajectory shows clearly that the O–O bond is much less stable in the superoxide  ${\rm O_2}^{-1}$  because it fluctuates much more. Therefore, the superoxide can dissociate more easily than the peroxide and damage the perovskite structure.

To further investigate perovskite stability upon exposure to oxygen and light, we computed the canonically averaged standard deviations of atomic positions in the four systems, by grouping atom i into MA, Pb/I, and O components:  $\sigma_i = \sqrt{\langle (\vec{r_i} - \langle \vec{r_i} \rangle)^2 \rangle}$ . Here,  $r_i$  stands for the location of atom i, and the angular bracket represents ensemble averaging. As shown in Table 1, the computed standard deviations in the

Table 1. Standard Deviations (Å) in Positions of the Atoms in the Pristine MAPbI<sub>3</sub>,  $O_2$ ,  $O_2^{-1}$ , and  $O_2^{-2}$  Systems<sup>a</sup>

	total <sup>b</sup>	$MA^c$	Pb-I <sup>d</sup>	O <sup>e</sup>
$MAPbI_3$	0.748	0.995	0.255	
$O_2$	0.760	1.016	0.263	0.280
$O_2^{-1}$	0.925	1.228	0.337	0.314
$O_2^{-2}$	0.995	1.316	0.375	0.315

 $^a{\rm The~fluctuations}$  are larger in the  ${\rm O_2}^{-1}$  and  ${\rm O_2}^{-2}$  systems, indicative of their reduced chemical stability.  $^b{\rm Averaged}$  over all atoms.  $^c{\rm Averaged}$  over atoms in MA.  $^d{\rm Averaged}$  over Pb and I atoms.  $^e{\rm Averaged}$  over O atoms.

positions of all atoms as well as each component grow in the sequence  $MAPbI_3 < O_2 < O_2^{-1} < O_2^{-2}$ , indicating that the structural stability decreases in this order. In particular, the values for the  $O_2$  systems increase slightly compared to the pristine  $MAPbI_3$ , rationalizing the experimental observation that perovskites exposed to oxygen degrade slowly in the dark environment. The atomic fluctuations are more significant in the superoxide and peroxide systems because interaction of negative oxygens with surrounding Pb atoms undermines perovskite structure, leading to higher chemical activity and reduced chemical stability.

**3.2. Electronic Structure.** Figure 4 shows the spin-down projected density of states (PDOS) of the pristine MAPbI<sub>3</sub>, O<sub>2</sub>,  $O_2^{-1}$ , and  $O_2^{-2}$  systems computed by using the optimized geometries. The  $O_2$ ,  $O_2^{-1}$ , and  $O_2^{-2}$  systems have 652, 653, and 654 valence electrons, and the calculated magnetic moments of these systems are 1.9938, 0.9985, and -0.0020, respectively. The values agree with the number of the unpaired electron(s) in the three systems. In particular, the lowest energy state of the O<sub>2</sub> molecule is triplet, and therefore the O<sub>2</sub> system is in the triplet state. The spin-down charge densities of the trap states, the VB maximum (VBM), and CB minimum (CBM) involved in the charge trapping and recombination processes are presented in the insets of Figure 4. The charge densities of the trap states are strongly localized around the oxygen species. The PDOS is split into contributions from the MA, Pb, I, and O components. Figure 4a shows that the CBM and the VBM of the pristine MAPbI3 are separated by a wide bandgap of 1.65 eV, consistent with the experiments<sup>64</sup> and other DFT values.<sup>65,66</sup> Introduction of an oxygen molecule into the pristine MAPbI3 has little effect on the bandgap regardless of its oxidation state (Figure 4b-d); however, midgap states are introduced by O2 and O2-1. The CBM is formed by Pb orbitals in all four systems, without oxygen

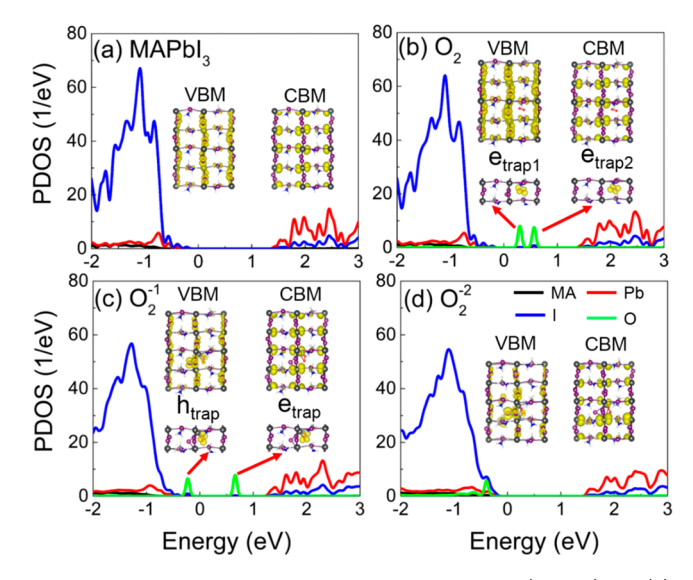


**Figure 4.** Spin-down projected densities of states (PDOS) of (a) pristine MAPbI<sub>3</sub>, (b)  $O_2$ , (c)  $O_2^{-1}$ , and (d)  $O_2^{-2}$  systems. The Fermi energy is set to zero. Spin-down charge densities of the key electronic states involved in the charge trapping and recombination processes are shown in the insets.

contributions. This is not the case for the VBM. The VBM originates from I orbitals in the pristine MAPbI<sub>3</sub>. This feature remains true in the O2 system because the neutral oxygen molecule interacts weakly with the inorganic lattice. Importantly, the oxygen molecule creates two deep electron trap states within the bandgap, marked by  $e_{\text{trap}2}$  for the state closest to the CBM and e<sub>trap1</sub> below e<sub>trap2</sub> (Figure 4b). The two trap states are localized entirely on the oxygen atoms and are strongly coupled to each other. The electron-hole recombination can occur either between the midgap states and the VBM or between the CBM electron and the VBM bypassing the electron trap states. In contrast to the molecular oxygen, the strong interactions between the super/peroxide species and the inorganic octahedra, mediated by the formed O-Pb chemical bonds, allow oxygen orbitals to contribute secondarily to the VBM (Figures 4c,d). The extra electron in  $O_2^{-1}$ breaks the near degeneracy of the two trap states seen in the O2 system. One of the trap states becomes populated, moves below the Fermi level, and becomes a hole trap (h<sub>trap</sub>) (Figure 4c). The other trap state  $(e_{trap})$  moves closer to the CBM. In this case, it is expected that the electron-hole recombination is accelerated with simultaneous assistance of both hole and electron traps. Introduction of two electrons eliminates the trap states in the  $O_2^{-2}$  system because the oxygen levels are lowered below the VBM (Figure 4d). As a result, the electronhole recombination in the  $O_2^{-2}$  system occurs via transitions between the CBM and the VBM, as in the pristine MAPbI<sub>3</sub>.

The charge trapping and recombination are directly dependent on the NA coupling matrix element between the initial and final wave functions,  $\langle \phi_i | \nabla_R | \phi_j \rangle$ . This matrix element requires overlap of the initial and final states. The inset of Figure 4a shows that the VBM and the CBM are supported by I and Pb, respectively. The situation minimizes wave functions mixing and generates small NA coupling, leading to a long excited-state lifetime. The charge distribution of the CBM remains largely unchanged in the three oxygen systems compared to the pristine MAPbI<sub>3</sub> and has little influence on changes in the NA coupling. The variation of the NA coupling

Table 2. Canonically Averaged Energy Gap, Absolute Value of NA Coupling, Pure-Dephasing Time, Nonradiative Charge Trapping and Recombination Times, and Radiative Lifetime for the VBM-CBM Transition in the Pristine MAPbI<sub>3</sub>,  $O_2$ ,  $O_2^{-1}$ , and  $O_2^{-2}$  Systems

		gap (eV)	NA coupling (meV)	dephasing (fs)	recombination (ps)	radiative lifetime (ns)
$MAPbI_3$	CBM-VBM	1.65	0.75	11.0	1820	7.28
$O_2$	$CBM-e_{trap2}$	1.22	1.72	4.74	0.80	
	CBM-e <sub>trap1</sub>	1.34	2.11	4.68	0.70	
	CBM-VBM	1.68	1.20	18.4	58.7	3.53
	$e_{trap2} - e_{trap1}$	0.12	7.56	17.5		
	e <sub>trap2</sub> -VBM	0.46	4.67	5.40	60.1	
	e <sub>trap1</sub> -VBM	0.34	11.9	5.26	50.6	
$O_2^{-1}$	CBM-e <sub>trap</sub>	1.24	2.19	3.22	1.00	
	CBM-h <sub>trap</sub>	1.49	2.09	4.19	3.90	
	CBM-VBM	1.74	0.76	13.2	7.60	2.77
	$e_{trap}-h_{trap}$	0.25	10.8	8.00		
	e <sub>trap</sub> -VBM	0.50	10.4	3.35	7.90	
	h <sub>trap</sub> -VBM	0.25	16.4	4.54	1.00	
$O_2^{-2}$	CBM-VBM	1.65	0.60	9.88	4280	8.94

arises from changes in the localization of the VBM, which attain oxygen contributions in the  ${\rm O_2}^{-1}$  and  ${\rm O_2}^{-2}$  systems, and on the properties of the trap states. In addition, generally, the NA coupling is inversely proportional to the energy gap: the smaller the gap, the larger the coupling. The VBM of the  ${\rm O_2}$  system has no oxygen contributions and is similar to the VBM of the pristine MAPbI<sub>3</sub>, while the trap states are fully localized on  ${\rm O_2}$  (inset in Figure 4b). The resulting pattern of the NA values is rather complex (Table 2). The small energy gap enhances the NA coupling between the electron/hole trap states and/or the band edge states in the superoxide. The peroxide localizes strongly the VBM onto itself, while decreases its localization on the other parts of the system. The feature decreases the VBM–CBM overlap, leading to a small NA coupling compared to the pristine MAPbI<sub>3</sub> (Table 2).

3.3. Electron-Vibrational Interactions. To characterize the phonon modes participating in the charge trapping and recombination, we computed the influence spectra in the spindown channel by performing Fourier transforms (FTs) of the energy gap fluctuations of the pairs of states. The intensity of each peak in the FTs reflects the strength of electronvibrational interaction at a given phonon frequency. The lowfrequency modes play the dominant role in the spectra (Figure 5a-d). The major peaks around 100 cm<sup>-1</sup> can be attributed to the stretching and bending modes of the I-Pb bonds. 67,68 The NA coupling is created by these modes. The peaks near 130 cm<sup>-1</sup> are associated with librations of the organic cations.<sup>68</sup> The peaks around and above 200 cm<sup>-1</sup> can be assigned to the C-N torsion of the MA cations.<sup>67</sup> All these modes are present in the four systems under investigation. The peaks around 150 cm<sup>-1</sup> in the MAPbI<sub>3</sub> containing various oxygen species can be interpreted as vibration of the O-Pb chemical bond.<sup>69</sup> The presence of this mode in the O2 system indicates that thermal fluctuations can bring the interstitial oxygen molecule to interact with the neighboring lead atoms at room temperature. The intensities of the phonon signals originated from the MA cations are notably weaker than those of the inorganic lattice because MA do not contribute to the key states and affect the electron-vibrational interactions indirectly though the created electric fields.

Quantum decoherence plays an extremely important role in influencing the charge-phonon dynamics. In general, shorter decoherence favors slower quantum dynamics. Quantum

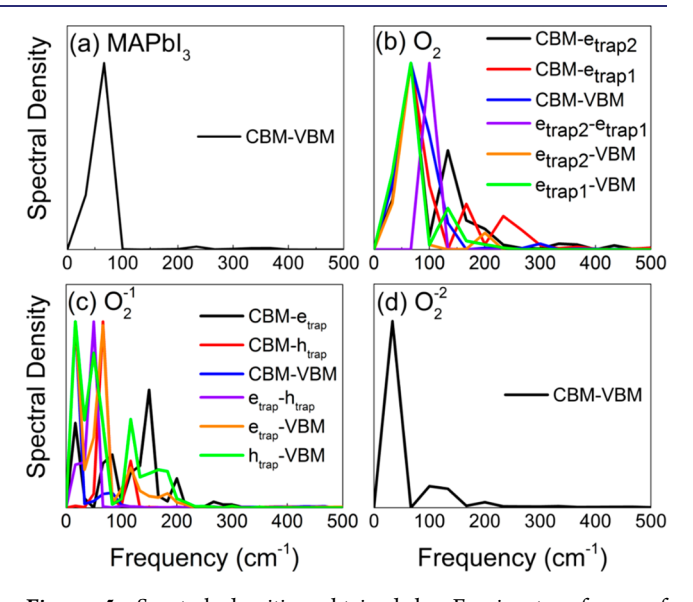


**Figure 5.** Spectral densities obtained by Fourier transforms of autocorrelation functions for the energy gap fluctuations in the pristine MAPbI<sub>3</sub>,  $O_2$ ,  $O_2^{-1}$ , and  $O_2^{-2}$  systems.

transition stops if the decoherence time is close to infinitesimal, as exemplified by the quantum Zeno effect. The decoherence time is estimated as the pure dephasing of the optical response theory using the second cumulant approximation. Loss of coherence breaks the superpositions formed between pairs of electronic states via NA coupling. The computed pure-dephasing times summarized in Table 2 range from several to tens of femtoseconds and are orders of magnitude smaller than the electron—hole recombination times. Therefore, the decoherence effects have to be included into the NAMD simulations. The strong peak intensities in the influence spectra as well as the presence of multiple phonon modes lead to shorter decoherence times (Table 2).

**3.4.** Nonradiative Charge Trapping and Recombination. Finally, we analyze the charge trapping and recombination dynamics in the pristine MAPbI<sub>3</sub>,  $O_2$ ,  $O_2^{-1}$ , and  $O_2^{-2}$  systems. As discussed in section 3.2,  $O_2$  and  $O_2^{-1}$  create midgap states, while  $O_2^{-2}$  removes them by pushing the oxygen-related states to the valence band. Therefore, it is expected that defect-mediated electron—hole recombination

plays a dominant role in the  $O_2$  and  $O_2^{-1}$  systems and that the recombination is faster than in the pristine system. In contrast, the recombination in the  $O_2^{-2}$  system takes places between the CBM and the VBM and is suppressed relative to pristine MAPbI<sub>3</sub> because of the smaller NA coupling and the shorter pure-dephasing time. The evolution of the populations of the key states is presented in Figure 6. Fitting the data with an

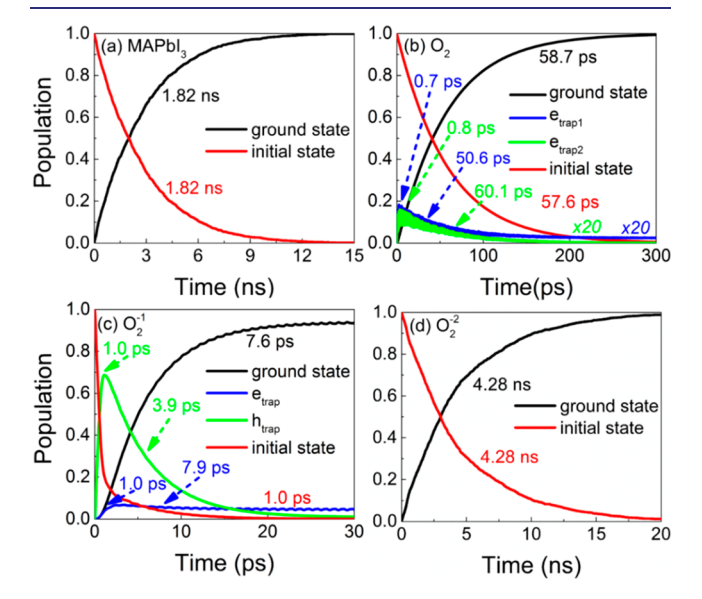


**Figure 6.** Charge trapping and recombination dynamics in the pristine MAPbI<sub>3</sub>,  $O_2$ ,  $O_2^{-1}$ , and  $O_2^{-2}$  systems. The electron trapping and detrapping processes are magnified 20 times in the  $O_2$  system.

exponential function,  $P(t) = \exp\left(-\frac{t}{\tau}\right)$ , gives the time scales in Figure 6 and Table 2. The rise and decay components of the populations for the trap states are fitted separately. The oxygen chemistry indeed has a strong influence on the charge carrier dynamics in perovskites. In particular, the neutral oxygen molecule and the superoxide accelerate the nonradiative electron—hole recombination, while the peroxide suppresses it compared to the pristine MAPbI<sub>3</sub>, in which charges relax within several nanoseconds, in agreement with experiment. The long charge carrier lifetimes in MAPbI<sub>3</sub> is due to the weak NA coupling and short pure-dephasing/decoherence time (Figure 6a and Table 2).

The oxygen molecule creates two deep electron trap states  $(e_{trap1}, e_{trap2})$ , which provide new nonradiative relaxation channels. Because the NA couplings of CBM/ $e_{trap1}$  and CBM/ $e_{trap2}$  are strong, and the two trap states are almost degenerate (Figure 4b and Table 2), the states provide two additional pathways for electron relaxation. Because the electron trap states are energetically far from the CB, the trap mediated and direct recombination between the CBM and VBM occur in parallel. Once electrons populate the trap states, they recombine with VB holes within 100 ps (Figure 6b). Even though a neutral oxygen atmosphere undermines slightly the perovskite chemical stability, the appearance of the charge trap states has a stronger effect on the perovskite performance because the traps notably shorten the charge carrier lifetimes.

The superoxide has an even stronger effect on the charge carriers. The presence of electron and hole trap states makes the recombination over 2 orders of magnitude faster compared to the pristine system (Figure 6c). The hole trapping assisted recombination is dominant because the energy gap between

 $h_{trap}$  and the VBM is small and the NA is large compared to the corresponding values between  $e_{trap}$  and the CBM (Table 2). Once holes populate the trap state, they recombine with the CB electrons within under 10 ps. The greatly shortened charge carrier lifetimes caused by the superoxide demonstrate that superoxide formation cannot be the origin of the observed improvement of the optical properties of perovskites exposed to oxygen atmosphere or pure oxygen.

In contrast to the superoxide, the peroxide eliminates the trap states and even extends the carrier lifetimes more than 2-fold relative to pristine MAPbI<sub>3</sub> because it reduces the NA coupling and shortens the quantum coherence time (Figure 6d and Table 2). The observed effects of the simultaneous exposure of HOIPs to oxygen and light are well explained by the calculated properties of the peroxide system. Just as in the experiments, the carrier lifetimes are enhanced in the peroxide presence, as demonstrated by the NAMD simulation, while the MAPbI<sub>3</sub> stability is decreased, as evidenced by the enhanced atomic fluctuations (Table 1). Because carrier losses are over 2 orders of magnitude faster in the presence of the superoxide compared to the peroxide, and the O–O bond is much less stable (Figure 3), reduction of the superoxide to the peroxide is highly desirable.

The above analysis focuses on the spin-down component of PDOS (Figure 4) because only the spin-down component exhibits midgap states. Neither oxygen species (O2, O2-1, O2<sup>-2</sup>) creates midgap states in the spin-up PDOS, shown in Figures S1 and S2 of the Supporting Information. The electron—hole recombination in the spin-up component occurs directly between the CBM and the VBM and is determined by the corresponding values of the NA coupling and the puredephasing time. The CBM and VBM charge densities presented in the insets of Figure S1 rationalize the trends in the NA coupling for spin-up component in the four systems under investigation (Table S1). The electron-hole recombination proceeds faster in the  $O_2$  and  $O_2^{-1}$  systems and slower in the  $O_2^{-2}$  system compared to pristine MAPbI<sub>3</sub>, as evidenced by the evolution of the populations shown in Figure S4 and the data presented in Table S1. Though the detailed mechanism for the electron-hole recombination for the spin-up channel differs from that in the spin-down channel, the key conclusions remain unchanged. The neutral oxygen molecule and the superoxide accelerate the recombination, while the peroxide slows it down.

Spin-orbit coupling (SOC) is significant in MAPbI<sub>3</sub> because it contains heavy elements, Pb and I. The spin-up and spin-down channels are coupled by SOC, and spins can be flipped during the charge trapping and recombination processes. Because the midgap trap states appear only in the spin-down components, there are no spin flips as the charges relax through the trap states. Therefore, the main influence of the oxygen species on the charge trapping and relaxation is independent of spin flips, to a good approximation. Because trap states are separated from band edges by significant energy gaps, while spin-up and spin-down states inside bands are essentially degenerate, spin flips are much more likely to occur inside bands than during trapping. If a charge in a band has spin-up, while a trap state is spin-down, the charge flips its spin while still inside the band and then hops into the trap state. It is important to note that a more rigorous analysis requires calculations beyond the single-particle description, for instance, via the linear response TDDFT description of excited states.

Unfortunately, such calculations are still too expensive to couple to ab initio NAMD on large systems.

To establish that the excited state lifetimes are limited by nonradiative rather than radiative decay, we estimated the radiative lifetimes for the pristine MAPbI<sub>3</sub>,  $O_2$ ,  $O_2^{-1}$ , and  $O_2^{-2}$  systems by calculating the Einstein coefficient of spontaneous emission. The computational details are presented in the Supporting Information. The calculated radiative lifetimes for the spin-down and spin-up channels, shown in Table 2 and Table S1, are longer than the nonradiative recombination times. Therefore, nonradiative electron—hole recombination constitutes the main process responsible for excited state decay.

Our final test focuses on the PBE functional. Pure DFT functionals, such as PBE, introduce the electron self-interaction error, and more rigorous theories such as hybrid functionals or the GW theory are required to eliminate the error. The GW theory or a hybrid functional significantly overestimates the bandgap in lead halide perovskites. To achieve good results, these more advanced DFT descriptions should be combined with SOC. 73 It is important to note that SOC discussed here differs from the SOC matrix elements that can cause spin flips discussed above. Incorporation of SOC into band structure calculations mixes spin-up and spin-down components, making the single particle orbitals into spinors. The resulting bandgap decreases greatly. If SOC is included in combination with PBE, the MAPbI<sub>3</sub> bandgap is grossly underestimated and becomes 0.56 eV,<sup>74</sup> nearly 3 times smaller than the experimental value of 1.52 eV.58 Fortuitous cancellation of the self-interaction error with the absence of SOC allows PBE to produce good bandgap values in lead halide perovskites. Such an approach allowed us to obtain good results while studying photoinduced dynamics in MAPbI<sub>3</sub> containing dopants, 75 grain boundaries, 76 localized charges,<sup>77</sup> and interfaces with water<sup>78</sup> and TiO<sub>2</sub>. Calculations combining SOC with the GW theory or a hybrid functional for a periodic system are too computationally demanding to be combined with NAMD.

We used GW+SOC to test the PBE results. GW theory is generally preferable over hybrid functionals because the fraction of the Hartree–Fock exchange is an adjustable parameter in hybrid functionals, while the GW theory has no such parameter. We constructed a 48-atom supercell for the  $O_2$ ,  $O_2^{-1}$ , and  $O_2^{-2}$  systems, optimized the system geometries using PBE+SOC with multiple k-points, and applied GW +SOC at the  $\Gamma$ -point due to high computational cost. Using only the  $\Gamma$ -point provides a good approximation because MAPbI $_3$  has a direct band gap at the  $\Gamma$ -point and because properties of isolated point defects are independent of k-point.

The PDOS and charge densities of the key states calculated with GW+SOC are shown in Figure S3. As in the PBE calculation without SOC,  $O_2$  introduces two electron trap states,  $O_2^{-1}$  introduces one electron trap, and  $O_2^{-2}$  creates no midgap traps. The trap states are closer to the bands than in the PBE calculations. In such a situation, the charge trapping will proceed faster, while the overall recombination will be slower than with deeper trap states. Still, the overall conclusions remain the same.  $O_2$  and  $O_2^{-1}$  introduce trap states that lead to charge trapping and accelerate recombination compared to pristine MAPbI<sub>3</sub>.  $O_2^{-2}$  introduces no trap states, and therefore it favors long-lived charge carriers.

#### 4. CONCLUSIONS

By performing ab initio real-time TDDFT simulations combined with NAMD, we have uncovered the atomistic origin of the extended charge carrier lifetimes and enhanced perovskite degradation in the presence of both atmospheric oxygen and light irradiation. Focusing on the pristine MAPbI<sub>3</sub> and MAPbI<sub>3</sub> containing the neutral  $O_2$ , superoxide  $O_2^{-1}$ , and peroxide  $O_2^{-2}$  species, our simulations demonstrate clearly that the photoinduced dynamics and stability of MAPbI<sub>3</sub> depend strongly on the oxidation state of the oxygen species.

The neutral oxygen molecule has little influence on the perovskite stability since it interacts weakly with MAPbI<sub>3</sub>. In contrast, the superoxide boosts degradation by breaking inorganic Pb–I bonds, resulting from O–O bond dissociation followed by O–Pb bond formation. The degradation is accelerated further when the superoxide is reduced to the peroxide since the doubly negative charge of  ${\rm O_2}^{-2}$  repulses iodine anions and attracts lead cations more strongly.

The neutral oxygen molecule creates two electron trap states within the fundamental energy gap, creating additional pathways for the nonradiative charge relaxation and accelerating the charge recombination to under 100 ps compared to over 1 ns in the pristine MAPbI3, in agreement with experiment.<sup>30</sup> The superoxide generates an electron trap state far away from the CBM and a hole trap state closer to the VBM. The nonradiative relaxation starts with a rapid hole trapping, and the possibility of simultaneous electron and hole trapping accelerates charge carrier losses by over 2 orders of magnitude. The acceleration of the charge carrier relaxation in both neutral and superoxide forms of oxygen is attributed to reduced energy gaps and enhanced NA coupling. Importantly, formation of the peroxide in MAPbI<sub>3</sub> eliminates trap states and reduces the electron-hole recombination rate by more than a factor of 2 compared to the pristine system. The extended lifetime arises due to decreased NA coupling and shortened quantum coherence time.

Both the superoxide and the peroxide cause perovskite degradation, while only the peroxide extends charge carrier lifetimes. Therefore, the superoxide should be strongly avoided during material synthesis and device fabrication. Because the detrimental superoxide can be photochemically reduced into the more benign peroxide, one may expect better perovskite performance at higher light fluences.

The study has rationalized the surprising experimental observations of the dual role of simultaneous exposure of metal halide perovskites to light and oxygen, leading to lower chemical stability but better electron-optical response. The study has established the detailed atomistic mechanisms of the charge trapping and recombination dynamics of the oxygen-doped perovskite and has demonstrated an extremely strong dependence on the oxidation state of the oxygen species. The reported results can apply to other photovoltaic energy conversion materials, which operate in the presence of both sunlight and atmosphere, the performance of which often depends on such exposure.

# ■ ASSOCIATED CONTENT

#### Supporting Information

The Supporting Information is available free of charge at https://pubs.acs.org/doi/10.1021/jacs.0c06769.

Details of calculations of radiative lifetimes, and data for the spin-up channel, including projected densities of states, charge densities of key orbitals, and electron-hole recombination dynamics (PDF)

#### AUTHOR INFORMATION

#### **Corresponding Author**

Run Long — College of Chemistry, Key Laboratory of Theoretical & Computational Photochemistry of Ministry of Education, Beijing Normal University, Beijing 100875, P. R. China; orcid.org/0000-0003-3912-8899; Email: runlong@bnu.edu.cn

#### **Authors**

Jinlu He — College of Chemistry, Key Laboratory of Theoretical & Computational Photochemistry of Ministry of Education, Beijing Normal University, Beijing 100875, P. R. China

Wei-Hai Fang — College of Chemistry, Key Laboratory of Theoretical & Computational Photochemistry of Ministry of Education, Beijing Normal University, Beijing 100875, P. R. China

Oleg V. Prezhdo — Department of Chemistry, University of Southern California, Los Angeles, California 90089, United States; Occid.org/0000-0002-5140-7500

Complete contact information is available at: https://pubs.acs.org/10.1021/jacs.0c06769

#### **Notes**

The authors declare no competing financial interest.

# ACKNOWLEDGMENTS

This work was supported by the National Science Foundation of China (Grants 21573022, 51861135101, 21688102, 21590801, and 21520102005). R.L. acknowledges the Recruitment Program of Global Youth Experts of China and the Beijing Normal University Startup. O.V.P. acknowledges funding from the U.S. National Science Foundation (Grant CHE-1900510).

# REFERENCES

- (1) Kojima, A.; Teshima, K.; Shirai, Y.; Miyasaka, T. Organometal Halide Perovskites as Visible-Light Sensitizers for Photovoltaic Cells. *J. Am. Chem. Soc.* **2009**, *131*, 6050–6051.
- (2) NREL: Efficiency Chart. https://www.nrel.gov/pv/cell-efficiency.html.
- (3) Liao, W.; Zhao, D.; Yu, Y.; Shrestha, N.; Ghimire, K.; Grice, C. R.; Wang, C.; Xiao, Y.; Cimaroli, A. J.; Ellingson, R. J.; Podraza, N. J.; Zhu, K.; Xiong, R.-G.; Yan, Y. Fabrication of Efficient Low-Bandgap Perovskite Solar Cells by Combining Formamidinium Tin Iodide with Methylammonium Lead Iodide. *J. Am. Chem. Soc.* **2016**, *138*, 12360–12363.
- (4) Pazos-Outón, L. M.; Szumilo, M.; Lamboll, R.; Richter, J. M.; Crespo-Quesada, M.; Abdi-Jalebi, M.; Beeson, H. J.; Vrućinić, M.; Alsari, M.; Snaith, H. J.; et al. Photon Recycling in Lead Iodide Perovskite Solar Cells. *Science* **2016**, *351*, 1430–1433.
- (5) Shi, D.; Adinolfi, V.; Comin, R.; Yuan, M.; Alarousu, E.; Buin, A.; Chen, Y.; Hoogland, S.; Rothenberger, A.; Katsiev, K.; et al. Low Trap-State Density and Long Carrier Diffusion in Organolead Trihalide Perovskite Single Crystals. *Science* **2015**, 347, 519–522.
- (6) Tian, W.; Leng, J.; Zhao, C.; Jin, S. Long-Distance Charge Carrier Funneling in Perovskite Nanowires Enabled by Built-in Halide Gradient. J. Am. Chem. Soc. 2017, 139, 579–582.
- (7) Stranks, S. D.; Snaith, H. J. Metal-Halide Perovskites for Photovoltaic and Light-Emitting Devices. *Nat. Nanotechnol.* **2015**, *10*, 391–402.

- (8) Li, Y. J.; Lv, Y.; Zou, C.-L.; Zhang, W.; Yao, J.; Zhao, Y. S. Output Coupling of Perovskite Lasers from Embedded Nanoscale Plasmonic Waveguides. J. Am. Chem. Soc. 2016, 138, 2122–2125.
- (9) Niu, G.; Guo, X.; Wang, L. Review of Recent Progress in Chemical Stability of Perovskite Solar Cells. *J. Mater. Chem. A* **2015**, 3, 8970–8980.
- (10) Han, Y.; Meyer, S.; Dkhissi, Y.; Weber, K.; Pringle, J. M.; Bach, U.; Spiccia, L.; Cheng, Y.-B. Degradation Observations of Encapsulated Planar CH<sub>3</sub>NH<sub>3</sub>PbI<sub>3</sub> Perovskite Solar Cells at High Temperatures and Humidity. *J. Mater. Chem. A* **2015**, *3*, 8139–8147.
- (11) Yang, J.; Siempelkamp, B. D.; Liu, D.; Kelly, T. L. Investigation of CH<sub>3</sub>NH<sub>3</sub>PbI<sub>3</sub> Degradation Rates and Mechanisms in Controlled Humidity Environments Using in Situ Techniques. *ACS Nano* **2015**, 9, 1955–1963.
- (12) Berhe, T. A.; Su, W.-N.; Chen, C.-H.; Pan, C.-J.; Cheng, J.-H.; Chen, H.-M.; Tsai, M.-C.; Chen, L.-Y.; Dubale, A. A.; Hwang, B.-J. Organometal Halide Perovskite Solar Cells: Degradation and Stability. *Energy Environ. Sci.* **2016**, *9*, 323–356.
- (13) Kim, H. S.; Seo, J. Y.; Park, N. G. Material and Device Stability in Perovskite Solar Cells. *ChemSusChem* **2016**, *9*, 2528–2540.
- (14) Senocrate, A.; Acartürk, T.; Kim, G. Y.; Merkle, R.; Starke, U.; Grätzel, M.; Maier, J. Interaction of Oxygen with Halide Perovskites. *J. Mater. Chem. A* **2018**, *6*, 10847–10855.
- (15) Sun, Q.; Fassl, P.; Becker-Koch, D.; Bausch, A.; Rivkin, B.; Bai, S.; Hopkinson, P. E.; Snaith, H. J.; Vaynzof, Y. Role of Microstructure in Oxygen Induced Photodegradation of Methylammonium Lead Triiodide Perovskite Films. *Adv. Energy Mater.* **2017**, *7*, 1700977.
- (16) Aristidou, N.; Sanchez-Molina, I.; Chotchuangchutchaval, T.; Brown, M.; Martinez, L.; Rath, T.; Haque, S. A. The Role of Oxygen in the Degradation of Methylammonium Lead Trihalide Perovskite Photoactive Layers. *Angew. Chem., Int. Ed.* **2015**, *54*, 8208–8212.
- (17) Tian, Y.; Peter, M.; Unger, E.; Abdellah, M.; Zheng, K.; Pullerits, T.; Yartsev, A.; Sundstrom, V.; Scheblykin, I. G. Mechanistic Insights into Perovskite Photoluminescence Enhancement: Light Curing with Oxygen Can Boost Yield Thousandfold. *Phys. Chem. Chem. Phys.* **2015**, *17*, 24978–24987.
- (18) Motti, S. G.; Gandini, M.; Barker, A. J.; Ball, J. M.; Srimath Kandada, A. R.; Petrozza, A. Photoinduced Emissive Trap States in Lead Halide Perovskite Semiconductors. ACS Energy Lett. 2016, 1, 726–730
- (19) Tian, Y.; Merdasa, A.; Unger, E.; Abdellah, M.; Zheng, K.; McKibbin, S.; Mikkelsen, A.; Pullerits, T.; Yartsev, A.; Sundstrom, V.; Scheblykin, I. G. Enhanced Organo-Metal Halide Perovskite Photoluminescence from Nanosized Defect-Free Crystallites and Emitting Sites. J. Phys. Chem. Lett. 2015, 6, 4171–4177.
- (20) Fu, X.; Jacobs, D. A.; Beck, F. J.; Duong, T.; Shen, H.; Catchpole, K. R.; White, T. P. Photoluminescence study of Time- and Spatial-Dependent Light Induced Trap De-Activation in CH<sub>3</sub>NH<sub>3</sub>PbI<sub>3</sub> Perovskite Films. *Phys. Chem. Chem. Phys.* **2016**, *18*, 22557–22564.
- (21) Bryant, D.; Aristidou, N.; Pont, S.; Sanchez-Molina, I.; Chotchunangatchaval, T.; Wheeler, S.; Durrant, J. R.; Haque, S. A. Light and Oxygen Induced Degradation Limits the Operational Stability of Methylammonium Lead Triiodide Perovskite Solar Cells. *Energy Environ. Sci.* **2016**, *9*, 1655–1660.
- (22) Zhang, L.; Sit, P. H. L. Ab Initio Study of the Role of Oxygen and Excess Electrons in the Degradation of CH<sub>3</sub>NH<sub>3</sub>PbI<sub>3</sub>. *J. Mater. Chem. A* **2017**, *5*, 9042–9049.
- (23) Ouyang, Y.; Li, Y.; Zhu, P.; Li, Q.; Gao, Y.; Tong, J.; Shi, L.; Zhou, Q.; Ling, C.; Chen, Q.; Deng, Z.; Tan, H.; Deng, W.; Wang, J. Photo-Oxidative Degradation of Methylammonium Lead Iodide Perovskite: Mechanism and Protection. *J. Mater. Chem. A* **2019**, *7*, 2275–2282.
- (24) Péan, E. V.; De Castro, C. S.; Dimitrov, S.; De Rossi, F.; Meroni, S.; Baker, J.; Watson, T.; Davies, M. L. Investigating the Superoxide Formation and Stability in Mesoporous Carbon Perovskite Solar Cells with an Aminovaleric Acid Additive. *Adv. Funct. Mater.* **2020**, *30*, 1909839.

- (25) He, J.; Fang, W. H.; Long, R.; Prezhdo, O. V. Superoxide/Peroxide Chemistry Extends Charge Carriers' Lifetime but Undermines Chemical Stability of CH<sub>3</sub>NH<sub>3</sub>PbI<sub>3</sub> Exposed to Oxygen: Time-Domain ab Initio Analysis. *J. Am. Chem. Soc.* **2019**, *141*, 5798–5807. (26) Akimov, A. V.; Prezhdo, O. V. The PYXAID Program for Non-Adiabatic Molecular Dynamics in Condensed Matter Systems. *J. Chem. Theory Comput.* **2013**, *9*, 4959–4972.
- (27) Akimov, A. V.; Prezhdo, O. V. Advanced Capabilities of the PYXAID Program: Integration Schemes, Decoherence Effects, Multiexcitonic States, and Field-Matter Interaction. *J. Chem. Theory Comput.* **2014**, *10*, 789–804.
- (28) Craig, C. F.; Duncan, W. R.; Prezhdo, O. V. Trajectory Surface Hopping in the Time-Dependent Kohn-Sham Approach for Electron-Nuclear Dynamics. *Phys. Rev. Lett.* **2005**, *95*, 163001.
- (29) Runge, E.; Gross, E. K. Density-Functional Theory for Time-Dependent Systems. *Phys. Rev. Lett.* **1984**, *52*, 997.
- (30) Klein, J. R.; Flender, O.; Scholz, M.; Oum, K.; Lenzer, T. Charge Carrier Dynamics of Methylammonium Lead Iodide: from PbI<sub>2</sub>-Rich to Low-Dimensional Broadly Emitting Perovskites. *Phys. Chem. Chem. Phys.* **2016**, *18*, 10800–10808.
- (31) Jaeger, H. M.; Fischer, S.; Prezhdo, O. V. Decoherence-Induced Surface Hopping. *J. Chem. Phys.* **2012**, *137*, 22A545.
- (32) Kohn, W.; Sham, L. J. Self-Consistent Equations Including Exchange and Correlation Effects. *Phys. Rev.* **1965**, *140*, A1133–A1138.
- (33) He, J.; Fang, W.-H.; Long, R. Weak Temperature-Dependent Hole Injection and Electron—Hole Recombination at the CH<sub>3</sub>NH<sub>3</sub>PbI<sub>3</sub>/NiO Heterojunction: A Time-Domain Ab Initio Study. J. Mater. Chem. A **2020**, 8, 607–615.
- (34) Zhang, Z.; Long, R. Doping-Induced Rapid Decoherence Suppresses Charge Recombination in Mono/Divalent Cation Mixed Perovskites from Nonadiabatic Molecular Dynamics Simulation. *J. Phys. Chem. Lett.* **2019**, *10*, 3433–3439.
- (35) Zhang, Z.; Fang, W. H.; Long, R.; Prezhdo, O. V. Exciton Dissociation and Suppressed Charge Recombination at 2D Perovskite Edges: Key Roles of Unsaturated Halide Bonds and Thermal Disorder. J. Am. Chem. Soc. 2019, 141, 15557–15566.
- (36) Wang, Y.; Long, R. Anomalous Temperature-Dependent Charge Recombination in CH<sub>3</sub>NH<sub>3</sub>PbI<sub>3</sub> Perovskite: Key Roles of Charge Localization and Thermal Effect. ACS Appl. Mater. Interfaces **2019**, 11, 32069–32075.
- (37) Jiang, Q.; Zhao, Y.; Zhang, X.; Yang, X.; Chen, Y.; Chu, Z.; Ye, Q.; Li, X.; Yin, Z.; You, J. Surface Passivation of Perovskite Film for Efficient Solar Cells. *Nat. Photonics* **2019**, *13*, 460–466.
- (38) Wang, Y.; He, J.; Yang, Y.; Zhang, Z.; Long, R. Chlorine Passivation of Grain Boundary Suppresses Electron—Hole Recombination in CsPbBr<sub>3</sub> Perovskite by Nonadiabatic Molecular Dynamics Simulation. ACS Appl. Energy Mater. **2019**, *2*, 3419–3426.
- (39) Wang, Y.; Fang, W. H.; Long, R.; Prezhdo, O. V. Symmetry Breaking at MAPbI<sub>3</sub> Perovskite Grain Boundaries Suppresses Charge Recombination: Time-Domain ab Initio Analysis. *J. Phys. Chem. Lett.* **2019**, *10*, 1617–1623.
- (40) Shi, R.; Long, R. Hole Localization Inhibits Charge Recombination in Tin-Lead Mixed Perovskites: Time-Domain ab Initio Analysis. *J. Phys. Chem. Lett.* **2019**, *10*, 6604–6612.
- (41) Qiao, L.; Fang, W. H.; Long, R. Ferroelectric Polarization Suppresses Nonradiative Electron-Hole Recombination in CH<sub>3</sub>NH<sub>3</sub>PbI<sub>3</sub> Perovskites: A Time-Domain ab Initio Study. *J. Phys. Chem. Lett.* **2019**, *10*, 7237–7244.
- (42) He, J.; Fang, W.-H.; Long, R. Unravelling the Effects of Oxidation State of Interstitial Iodine and Oxygen Passivation on Charge Trapping and Recombination in CH<sub>3</sub>NH<sub>3</sub>PbI<sub>3</sub> Perovskite: A Time-Domain Ab Initio Study. *Chem. Sci.* **2019**, *10*, 10079–10088.
- (43) Wang, S.; Fang, W. H.; Long, R. Hydrogen Passivated Silicon Grain Boundaries Greatly Reduce Charge Recombination for Improved Silicon/Perovskite Tandem Solar Cell Performance: Time Domain Ab Initio Analysis. *J. Phys. Chem. Lett.* **2019**, *10*, 2445–2452. (44) Yang, Y.; Fang, W. H.; Benderskii, A.; Long, R.; Prezhdo, O. V. Strain Controls Charge Carrier Lifetimes in Monolayer WSe<sub>2</sub>: Ab

- Initio Time Domain Analysis. J. Phys. Chem. Lett. 2019, 10, 7732-7739
- (45) Lu, T. F.; Wang, Y. S.; Tomko, J. A.; Hopkins, P. E.; Zhang, H. X.; Prezhdo, O. V. Control of Charge Carrier Dynamics in Plasmonic Au Films by TiO<sub>x</sub> Substrate Stoichiometry. *J. Phys. Chem. Lett.* **2020**, *11*, 1419–1427.
- (46) Qiao, L.; Fang, W. H.; Long, R.; Prezhdo, O. V. Extending Carrier Lifetimes in Lead Halide Perovskites with Alkali Metals by Passivating and Eliminating Halide Interstitial Defects. *Angew. Chem., Int. Ed.* **2020**, *59*, 4684–4690.
- (47) Tong, C. J.; Li, L. Q.; Liu, L. M.; Prezhdo, O. V. Synergy between Ion Migration and Charge Carrier Recombination in Metal-Halide Perovskites. *J. Am. Chem. Soc.* **2020**, *142*, 3060–3068.
- (48) Yang, Y. T.; Fang, W. H.; Benderskii, A.; Long, R.; Prezhdo, O. V. Strain Controls Charge Carrier Lifetimes in Monolayer WSe<sub>2</sub>: Ab Initio Time Domain Analysis. *J. Phys. Chem. Lett.* **2019**, *10*, 7732–7739.
- (49) Zhou, G. Q.; Cen, C.; Wang, S. Y.; Deng, M. S.; Prezhdo, O. V. Electron-Phonon Scattering Is Much Weaker in Carbon Nanotubes than in Graphene Nanoribbons. *J. Phys. Chem. Lett.* **2019**, *10*, 7179–7187.
- (50) Li, W.; Vasenko, A. S.; Tang, J. F.; Prezhdo, O. V. Anharmonicity Extends Carrier Lifetimes in Lead Halide Perovskites at Elevated Temperatures. *J. Phys. Chem. Lett.* **2019**, *10*, 6219–6226.
- (51) Li, W.; Long, R.; Tang, J. F.; Prezhdo, O. V. Influence of Defects on Excited-State Dynamics in Lead Halide Perovskites: Time-Domain ab Initio Studies. *J. Phys. Chem. Lett.* **2019**, *10*, 3788–3804.
- (52) Chaban, V. V.; Prezhdo, V. V.; Prezhdo, O. V. Covalent Linking Greatly Enhances Photoinduced Electron Transfer in Fullerene-Quantum Dot Nanocomposites: Time-Domain Ab Initio Study. *J. Phys. Chem. Lett.* **2013**, *4*, 1–6.
- (53) Wang, L. J.; Long, R.; Prezhdo, O. V. Time-Domain Ab Initio Modeling of Photoinduced Dynamics at Nanoscale Interfaces. *Annu. Rev. Phys. Chem.* **2015**, *66*, 549–579.
- (54) Åkimov, A. V.; Asahi, R.; Jinnouchi, R.; Prezhdo, O. V. What Makes the Photocatalytic  $CO_2$  Reduction on N-Doped  $Ta_2O_5$  Efficient: Insights from Nonadiabatic Molecular Dynamics. *J. Am. Chem. Soc.* **2015**, *137*, 11517–11525.
- (55) Li, L. Q.; Long, R.; Prezhdo, O. V. Charge Separation and Recombination in Two-Dimensional MoS2/WS2: Time-Domain ab Initio Modeling. *Chem. Mater.* **2017**, *29*, 2466–2473.
- (56) Long, R.; Casanova, D.; Fang, W. H.; Prezhdo, O. V. Donor Acceptor Interaction Determines the Mechanism of Photoinduced Electron Injection from Graphene Quantum Dots into TiO<sub>2</sub>:pi-Stacking Supersedes Covalent Bonding. *J. Am. Chem. Soc.* **2017**, *139*, 2619–2629.
- (57) Yang, Y.; Fang, W. H.; Long, R. Disparity in Photoexcitation Dynamics between Vertical and Lateral MoS<sub>2</sub>/WSe<sub>2</sub> Heterojunctions: Time-Domain Simulation Emphasizes the Importance of Donor-Acceptor Interaction and Band Alignment. *J. Phys. Chem. Lett.* **2017**, *8*, 5771–5778.
- (58) Stoumpos, C. C.; Malliakas, C. D.; Kanatzidis, M. G. Semiconducting Tin and Lead Iodide Perovskites with Organic Cations: Phase Transitions, High Mobilities, and Near-Infrared Photoluminescent Properties. *Inorg. Chem.* **2013**, *52*, 9019–9038.
- (59) Kresse, G.; Furthmüller, J. Efficient Iterative Schemes for Ab Initio Total-Energy Calculations Using A Plane-Wave Basis Set. *Phys. Rev. B: Condens. Matter Mater. Phys.* **1996**, *54*, 11169.
- (60) Perdew, J. P.; Burke, K.; Ernzerhof, M. Generalized Gradient Approximation Made Simple. *Phys. Rev. Lett.* **1996**, 77, 3865–3868.
- (61) Blöchl, P. E. Projector Augmented-Wave Method. *Phys. Rev. B: Condens. Matter Mater. Phys.* **1994**, *50*, 17953–17979.
- (62) Monkhorst, H. J.; Pack, J. D. Special Points for Brillouin-Zone Integrations. *Phys. Rev. B* **1976**, *13*, 5188–5192.
- (63) Grimme, S.; Antony, J.; Ehrlich, S.; Krieg, H. A Consistent and Accurate Ab Initio Parametrization of Density Functional Dispersion Correction (DFT-D) for the 94 Elements H-Pu. *J. Chem. Phys.* **2010**, 132, 154104.

- (64) Quarti, C.; Mosconi, E.; Ball, J. M.; D'Innocenzo, V.; Tao, C.; Pathak, S.; Snaith, H. J.; Petrozza, A.; De Angelis, F. Structural and Optical Properties of Methylammonium Lead Iodide across the Tetragonal to Cubic Phase Transition: Implications for Perovskite Solar Cells. *Energy Environ. Sci.* **2016**, *9*, 155–163.
- (65) Giorgi, G.; Fujisawa, J.-I.; Segawa, H.; Yamashita, K. Cation Role in Structural and Electronic Properties of 3D Organic—Inorganic Halide Perovskites: A DFT analysis. *J. Phys. Chem. C* **2014**, *118*, 12176—12183.
- (66) Yu, C.-J.; Jong, U.-G.; Ri, M.-H.; Ri, G.-C.; Pae, Y.-H. Electronic Structure and Photoabsorption Property of Pseudocubic Perovskites CH<sub>3</sub>NH<sub>3</sub>PbX<sub>3</sub> (X= I, Br) Including Van Der Waals Interaction. *J. Mater. Sci.* **2016**, *51*, 9849–9854.
- (67) Leguy, A. M.; Goñi, A. R.; Frost, J. M.; Skelton, J.; Brivio, F.; Rodríguez-Martínez, X.; Weber, O. J.; Pallipurath, A.; Alonso, M. I.; Campoy-Quiles, M.; et al. Dynamic Disorder, Phonon Lifetimes, and the Assignment of Modes to the Vibrational Spectra of Methylammonium Lead Halide Perovskites. *Phys. Chem. Chem. Phys.* **2016**, *18*, 27051–27066.
- (68) Quarti, C.; Grancini, G.; Mosconi, E.; Bruno, P.; Ball, J. M.; Lee, M. M.; Snaith, H. J.; Petrozza, A.; De Angelis, F. The Raman Spectrum of the CH<sub>3</sub>NH<sub>3</sub>PbI<sub>3</sub> Hybrid Perovskite: Interplay of Theory and Experiment. *J. Phys. Chem. Lett.* **2014**, *5*, 279–284.
- (69) Kong, W.; Rahimi-Iman, A.; Bi, G.; Dai, X.; Wu, H. Oxygen Intercalation Induced by Photocatalysis on the Surface of Hybrid Lead Halide Perovskites. *J. Phys. Chem. C* **2016**, *120*, 7606–7611.
- (70) Kilina, S. V.; Neukirch, A. J.; Habenicht, B. F.; Kilin, D. S.; Prezhdo, O. V. Quantum Zeno Effect Rationalizes the Phonon Bottleneck in Semiconductor Quantum Dots. *Phys. Rev. Lett.* **2013**, *110*, 180404.
- (71) Mukamel, S. Principles of Nonlinear Optical Spectroscopy; Oxford University Press: New York, 1995.
- (72) Liu, J.; Neukirch, A. J.; Prezhdo, O. V. Non-Radiative Electron—Hole Recombination in Silicon Clusters: Ab Initio Non-Adiabatic Molecular Dynamics. *J. Phys. Chem. C* **2014**, *118*, 20702—20709.
- (73) Amat, A.; Mosconi, E.; Ronca, E.; Quarti, C.; Umari, P.; Nazeeruddin, M. K.; Gratzel, M.; De Angelis, F. Cation-Induced Band-Gap Tuning in Organohalide Perovskites: Interplay of Spin-Orbit Coupling and Octahedra Tilting. *Nano Lett.* **2014**, *14*, 3608–3616.
- (74) Even, J.; Pedesseau, L.; Jancu, J.-M.; Katan, C. Importance of Spin—Orbit Coupling in Hybrid Organic/Inorganic Perovskites for Photovoltaic Applications. *J. Phys. Chem. Lett.* **2013**, *4*, 2999—3005.
- (75) Long, R.; Prezhdo, O. V. Dopants Control Electron-Hole Recombination at Perovskite-TiO<sub>2</sub> Interfaces: Ab Initio Time-Domain Study. ACS Nano 2015, 9, 11143–11155.
- (76) Long, R.; Liu, J.; Prezhdo, O. V. Unravelling the Effects of Grain Boundary and Chemical Doping on Electron-Hole Recombination in CH<sub>3</sub>NH<sub>3</sub>PbI<sub>3</sub> Perovskite by Time-Domain Atomistic Simulation. *J. Am. Chem. Soc.* **2016**, *138*, 3884–3890.
- (77) Zhang, Z.; Long, R.; Tokina, M. V.; Prezhdo, O. V. Interplay between Localized and Free Charge Carriers Can Explain Hot Fluorescence in the CH<sub>3</sub>NH<sub>3</sub>PbBr<sub>3</sub> Perovskite: Time-Domain Ab Initio Analysis. *J. Am. Chem. Soc.* **2017**, *139*, 17327–17333.
- (78) Long, R.; Fang, W.; Prezhdo, O. V. Moderate Humidity Delays Electron-Hole Recombination in Hybrid Organic-Inorganic Perovskites: Time-Domain Ab Initio Simulations Rationalize Experiments. *J. Phys. Chem. Lett.* **2016**, *7*, 3215–3222.
- (79) Long, R.; Fang, W.-H.; Prezhdo, O. V. Strong Interaction at the Perovskite/TiO<sub>2</sub> Interface Facilitates Ultrafast Photoinduced Charge Separation: A Nonadiabatic Molecular Dynamics Study. *J. Phys. Chem.* C **2017**, *121*, 3797–3806.